Engineering Fracture Mechanics 190 (2018) 16–30

Contents lists available at ScienceDirect

Engineering Fracture Mechanics

journal homepage: www.elsevier.com/locate/engfracmech

Fracture toughness of adhesively bonded joints with large plastic deformations

Xiang-Fa Wu *, Uraching Chowdhury

Department of Mechanical Engineering, North Dakota State University, Fargo, ND 58108, USA

ARTICLE INFO

Article history:
Received 26 September 2017
Received in revised form 19 November 2017
Accepted 29 November 2017
Available online 2 December 2017

Keywords:
Fracture toughness
Adhesively bonded joints (ABJs)
Double cantilever beam (DCB)
Elastoplastic deformation
Elastic springback

ABSTRACT

An elastoplastic fracture mechanics model is formulated for determining the fracture toughness of adhesively bonded joints (ABJs) with large plastic deformations and elastic springback. The analysis is made on the basis of the post-fracture configuration of double cantilever beam (DCB) specimen consisting of two adhesively bonded thin plates of ductile metals (*e.g.*, thin aluminum alloy or mild steel plates). Due to the springback after large plastic deformation, the post-fracture configuration of the adherends was noticeably different from that at the peak loading. To model the fracture process, the ductile metal adherends are treated as elastoplastic solids with power-law strain-hardening behavior, and springback of the adherends is considered in the strain energy calculation. The present model is capable of determining the fracture toughness of ABJs with extensive plastic deformation. Numerical simulations are performed to evaluate the effects of material parameters and specimen geometries on the springback and fracture toughness of the ABJs. Compared to the experimental data available in the literature, the present model can predict reliable fracture toughness of ABJs with large plastic deformations. The present study is applicable for the analysis of various fracture tests of thin ductile films with large plastic deformations and elastic springback such as peeling test, metal cutting, *etc.*

1. Introduction

Adhesively bonded joints (ABJs) have been used extensively in aerospace, aeronautical and ground vehicles for bonding and connecting thin structural parts, repairing surface defects, *etc.* [1–4]. A number of robust joint models have been formulated and implemented for joint design and strength analysis [5–9]. Superior to traditional mechanical joints, *e.g.*, bolted and welded joints, a major technological advantage of ABJs is their low material and labor costs, high joining strength and fatigue durability, efficient load-transferring capability, and noticeable weight reduction of the joining parts. In the view of structural integrity, bonding strength and fatigue durability are the dominate factors governing the mechanical performance of ABJs. Subjected to external loading, ABJs typically exhibit complicated stress and strain state due to their complex geometries and mismatch of material properties across the bonding lines of the adherends. Therefore, in-depth understanding of the strength and failure mechanisms of ABJs is crucial to better design and more reliable and predictable performance of engineered ABJs. So far, remarkable efforts have been dedicated to the investigation on the toughening and failure mechanisms ABJs made of metals and composite materials and related structural design and strength analysis [10–13].

* Corresponding author.
E-mail address: xiangfa.wu@ndsu.edu (X.-F. Wu).

https://doi.org/10.1016/j.engfracmech.2017.11.040
0013-7944/

Nomenclature

A	material constant of a power-law nonlinear elastic solid
h	adherend thickness of an adhesively bonded joint
E	Young's modulus
I	moment of inertia of the cross-section area of an adherend of unit width ($=h^3/12$)
M	bending moment acting on an adherend
M_c	critical bending moment to initiate yielding in adherends
n	exponent of a power-law nonlinear elastic solid; strain-hardening index of a power-law hardening solid
R_1, R_2	radii of curvature of two post-fracture adherends after springback
y	coordinate of a material point from the adherend neutral axis
y_c	location of the critical point between regions of plastic and elastic deformation
Γ	fracture toughness; strain energy release rate
Δl	crack growth length
ΔW_1, ΔW_2	work done by the bending moment acting on two adherends, *i.e.*, ΔW_i (i = 1,2)
ΔU_1, ΔU_2	strain energy stored in two adherends, *i.e.*, ΔU_i (i = 1,2)
$\Delta\varepsilon$	axial strain release at location y of a plastically deformed adherend after unloading [$=y(1/\rho_m-1/\rho)$]
ε	axial strain of an adherend
ε_0	axial yield strain ($=\sigma_0/E$)
ε_p	residual axial strain of a plastically deformed adherend after unloading
η	axial strain at adherend surface [$=h/(2\rho)$]
η_m	axial strain at adherend surface at the maximum bending moment [$=h/(2\rho_m)$]
ρ	radius of curvature of the adherend neutral axis at bending moment M
ρ_0	radius of curvature of the neutral axis of a plastically deformed adherend after unloading
ρ_m	radius of curvature of the neutral axis of a plastically deformed adherend at the maximum bending moment, *i.e.*, minimum radius of curvature
σ	flexural stress of an adherend
σ_0	yield strength
ABJ	adhesively bonded joint
CLS	cracked lap shear
DCB	double cantilever beam
ERR	(strain) energy release rate
FEM	finite element method
LEFM	linearly elastic fracture mechanics
PMC	polymer matrix composite
SSY	linearly elastic facture mechanics

In the view of structural applications, characterization and enhancement of the fracture toughness of ABJs are crucial to improve their structural integrity and safety. Quite a few efficient and reliable mechanical characterization techniques and related specimen designs have been formulated and standardized for evaluating the fracture toughness of ABJs, *e.g.*, those based on double cantilever beams (DCB), cracked lap shear specimens (CLS), four-point bending specimens, *etc.* [11,12]. Accordingly, substantial progress has been made in fracture mechanics of layered structures including those carrying the geometries close to ABJs. Systematic studies of mixed-mode cracks in layered materials and composites have been performed by Hutchinson and Suo [14,15] and others, in which the energy release rate (ERR) of crack initiation and propagation and related crack mode partition have been obtained with the aid of the elementary beam theory. These fundamental investigations have been extensively utilized for the analysis of interfacial fracture and buckling delamination in broad layered materials and structures including ABJs, surface coatings, ceramics, and laminated polymer matrix composites (PMCs). In addition, for the purpose of accurately predicting the mixed-mode crack growth in layered materials, crack-tip elements were formulated and integrated into conventional finite element methods (FEM) by Davidson, et al. [16–18]. The effect of crack tip deformation on mixed-mode crack growth in bonded layers was investigated by Wang and Qiao [19]. In addition, elasticity theories may be resorted for analyzing interfacial cracks embedded in thick beams. Yet, only a few simple cases of interfacial cracks embedded in elastic strips can be solved in explicit forms, *e.g.*, the cases of simple cracked strips treated by Wu et al. [20–23], and elastic solutions to more general cases of ABJs can be obtained in high accuracy by evoking efficient semi-analytic methods and purely numerical methods (*e.g.*, FEM).

Experimentally, the fracture toughness of ABJs can be determined by measuring the critical external force and displacement or the work done by external forces per unit crack growth. With the fracture test data, fracture mechanics and classic crack solutions can be utilized to extract the fracture toughness and crack mode partition. As a matter of fact, most crack

solutions to common fracture specimens available in the literature are obtained within the framework of linearly elastic fracture mechanics (LEFM), in which small-scale yield (SSY) is assumed at crack tip. Obviously, fracture of ABJs with large plastic deformation is beyond the consideration of LEFM while the fundamental concepts of fracture mechanics are still workable. When considering the fracture of ABJs made of thin ductile metal plates, plastic deformation in the ductile adherends contributes substantially to the energy dissipation and has to be taken into account for accurate estimate of the relevant fracture toughness [24–33]. In the special cases of nonlinear elastic solids, Atkins et al. [34] and Li and Lee [35] formulated the analytic solutions to the ERRs of DCB specimens. Yet, these crack models and solutions are not applicable for the realistic elastoplastic fracture with large plastic deformation and afterward elastic springback due to crack-growth induced unloading.

In their experimental studies, Thouless et al. [26] formulated an effective steady fracture test scheme for evaluating the fracture toughness of ABJs made of thin metal plates. In the test, a symmetric configuration of the fracture specimens of ABJs (Dimensions: 90 mm × 20 mm) was utilized, in which two identical aluminum-alloy (5754 aluminum, Alcan Rolled Products Co.) or mild-steel (draw-quality, special-killed, cold-rolled steel, Inland Steel Co. with a nominal yield stress of 170–240 MPa) plates were adhesively bonded, as shown in Fig. 1. Three commercially available toughened epoxies were used to bond the ductile metal plates, *i.e.*, adhesives *A* (Ciba-Geigy LMD1142), *B* (Ciba-Geiyy XD4600), and C (Essex 73,301), which were curved at 180 °C for 30 min. in an air-circulating oven [26]. The bond length of the ABJ specimens was 30.0 mm, which was established by placing a strip of Teflon tape (12.7 mm in width) across each adherend 30 mm from the ends of the adherend. The thickness of the adhesive layer was controlled by sprinkling a few glass beads of the diameter 0.25 mm on the adhesive. The ABJ specimens were clamped during curing, and the excess adhesives at the sides and end of the ABJs were filed off. The steady dynamic fracture test was performed at room temperature (21 °C) on an instrumented dynamic testing machine (Dynatup, General Research Corp., Model GRC 8250) based on a drop weight method. The testing specimen was positioned over a hardened steel wedge with a tip radius of 1 mm and a wedge angle of 10.0°. The tip of the wedge was kept to align with a locating mark scribed on the side surface of the ABJ specimen, 10 mm from the edge of the adhesive. The impactor force was generated by a mass of 44.85 kg, which pushed the wedge through the ABJ specimen, resulting in the two adherends to bend and the adhesive to fracture, as illustrated in Fig. 2. The impact speed upon striking the specimen was 2 ± 0.2 m/s. After the fracture test, the radii of curvature of the two post-fracture metal adherends carried a small variation due to the uncontrollable factors in the fracture event. The fracture toughness was determined conveniently by using a relation [26]:

$$\Gamma = \frac{An(h)^{n+2}}{2^n(n+2)(n+1)}\left(\frac{1}{R_1^{n+1}} + \frac{1}{R_2^{n+1}}\right). \tag{1}$$

In above, R_1 and R_2 are the radii of curvature measured from two post-fracture adherends of the ABJ specimen with large plastic deformations, h is the adherend thickness, and A and n are the material constants of the nonlinear elastic material model:

$$\sigma = A\varepsilon^n. \tag{2}$$

Thouless et al. [26] indicated that data reduction of the ABJ fracture tests based on relation (1) might result in the extracted fracture toughness only half the experimental values obtained in other control fracture tests. Kinloch and Williams [36,37] attributed such a large deviation of fracture toughness to the root rotation of the adherends during crack advance, which is incompatible with the steady fracture test method [38]. Further examination of the derivation of fracture toughness (1) shows that two potential factors may noticeably influence the extraction of the fracture toughness from the fracture test data as addressed in the late discussions [28,29,36–38]. First, Thouless et al. [26] used a nonlinear elastic material model to approach the material property of the well-ductile metals employed in their steady dynamic fracture tests. In fact, elastic springback of the fracture specimens after elastoplastic deformation was ignored in their calculation, which noticeably altered the radii of curvature of the adherends R_1 and R_2 as used in relation (1) by Thouless et al. [26]. The actual radii of curvature of the adherends at the maximum working moment (with the largest elastoplastic deformation) were much smaller than the ones measured from the post-fracture adherends after elastic springback, especially for those ABJs made of very thin ductile metal plates which bore very large plastic deformations and afterward large elastic springback. Thus, the theoretical simplification for the convenience of data reduction by Thouless et al. [26] might have noticeably underestimated the steady working moment that was consequently utilized for determining the fracture toughness of the ABJs. Second, due to

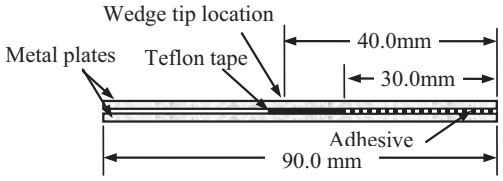

Fig. 1. Schematic configuration of a fracture specimen used by Thouless et al. [26] consists of two 90-mm length metal coupons of identical thickness, adhesively bonded with toughened epoxy over 30 mm at one side. The tip of the wedge is positioned at the left end of the Teflon tape at the beginning of the dynamic test.

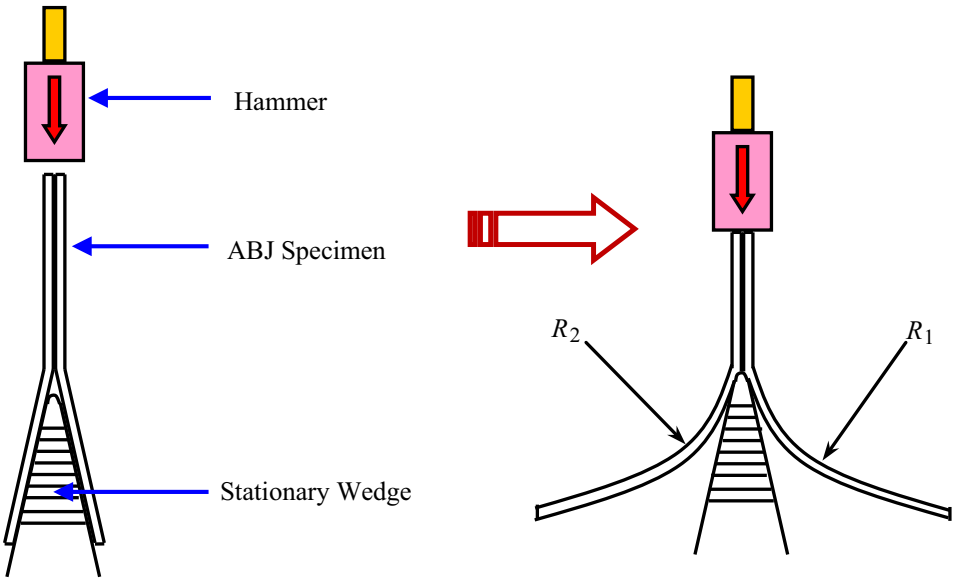

Fig. 2. Experimental configuration of the instrumented impact fracture test, in which the fracture ABJ specimen was split by being driven over a wedge under the low-speed moving hammer, and large elastoplastic deformation and afterward elastic springback exhibited.

the large elastic springback in the thin ductile adherends of the ABJs, the actual strain energy stored in the post-fracture adherends is appreciably lower than that calculated without elastic springback. Such a combined effect is expected to substantially underestimate the fracture toughness of the ABJs by using relation (1).

With the above knowledge of the fracture of ABJs with large plastic deformations, the goal of the present study is aimed to reinvestigate and resolve the large deviation between the experimental results and existing theoretical approach by adopting an elastoplastic material model with elastic springback to approach the loading and unloading mechanical behavior of ABJs made of thin metal plates in the fracture tests. During the procedure, based on the radii of curvature of the adherends measured from the post-fracture specimens, the adherend radii of curvature at the maximum working moment are to be determined via springback analysis of the adherends. The strain energy stored in the elastoplastically deformed adherends can be calculated in three terms, *i.e.*, the linearly elastic portion, the strain-hardening portion, and the unloading portion. The proposed elastoplastic fracture mechanics model will be utilized to extract the fracture toughness of ABJs with large plastic deformations based on the experimental fracture data reported in the literature [26]. Numerical experimentation will be performed to examine the elastic springback effect on the fracture toughness of ABJs with varying Young's modulus, yield stress, strain hardening index, and the specimen geometries. Discussions on the present fracture mechanics model and its comparison with those available in the literature will be further made.

2. Model formulation of ABJs with large plastic deformations and springback under pure bending

The analysis of steady dynamic fracture test of ABJs performed by Thouless et al. [26] was based on the work done by a wedge and the strain energy stored in the ABJ adherends after large nonlinear elastic deformation. In their model, the measured radii of curvature of the two elastoplastically deformed adherends of the ABJs were not corresponding the maximum working bending moment due to elastic springback. In addition, a substantial portion of the strain energy release was ignored due to the springback of the post-fracture adherends. As a result, the fracture toughness of the ABJs was determined by calculating the nonlinear elastic strain energy of the ABJs. Herein, both the large elastoplastic deformation and elastic springback of the ductile adherends of the ABJ specimens are to be considered. During the fracture event, both adherends of the ABJ specimens underwent loading and unloading. Large elastoplastic deflection happens at the bending root (crack tip) under the action of the working moment exerted by the wedge. The measured radii of curvature of the adherends are the ones after substantial elastic springback due to unloading. Springback results in the fact that the radii of curvature measured from the post-fracture adherends are much larger than the ones at the instant of the maximum working moment which drives the fracture event. Such a steady fracture scenario was ignored in extracting the fracture toughness of the tested ABJs made of thin ductile metal plates in the previous studies such that the actual steady elastoplastic fracture of ABJs was simplified as a process of nonlinear elastic process without obvious elastic springback [26,27,33,36–38]. Hereafter, for the purpose of the present modeling, the material properties of ABJs made of thin aluminum and steel plates are assumed to be elastoplastic solids following a power-law strain-hardening law [39]:

$$\sigma = \begin{cases} E\varepsilon, & (\sigma \leqslant \sigma_0) \\ \frac{\sigma_0}{(\sigma_0/E)^n}\varepsilon^n, & (\sigma > \sigma_0) \end{cases} \tag{3}$$

where E is the Young's modulus, σ_0 the yield strength for both tension and compression, and n is the strain-hardening index. The representative strain-stress curve is illustrated in Fig. 3. For $n \to 1$, the material model covers that of linearly elastic materials, while $n \to \infty$, the material model covers that of idealized elastoplastic materials.

Let us treat both the symmetric adherends of the ABJs as *Euler-Bernoulli* beams and the flexural strain in the beam cross-section of each adherend is linearly varying for both elastic and elastoplastic deformations:

$$\varepsilon = y/\rho, \tag{4}$$

where ρ is the radius of curvature of the neutral axis of each deflected adherend, and y is the distance from a material point of interest in the adherend cross-section to its neutral axis (*i.e.*, the mid-plane of the adherend), as shown in Fig. 4. The critical bending moment per unit specimen width to initiate the plastic deformation in each adherend is

$$M_c = \sigma_0 h^2/6. \tag{5}$$

Thus, given an external bending moment $M > M_c$, plastic deformation initiates and elastic springback is triggered once crack grows and unloading at crack tip happens.

Hereafter, we first determine the relationship between the bending moment M acting at one adherend and the corresponding radius of curvature ρ of the neutral axis of the adherend in the case of pure bending (loading and unloading). Based on the assumption of *Euler-Bernoulli* beam, the axial strain in the adherend linearly varies following relation (4), and the stress distribution follows relation (3). The locus y_c of the critical point, at which plastic deformation initiates, can be determined as

$$y_c = \rho\varepsilon_0, \tag{6}$$

where $\varepsilon_0 = \sigma_0/E$ is the yield strain. With the aid of the constitutive relation of the material as shown in Eq. (3), the relationship between the loading moment M (per unit width) and the resulting radius of curvature of the neutral axis is

$$\frac{M(\rho)}{EI/\rho} = \begin{cases} \left(1 - \frac{3}{n+2}\right)\left(\frac{\eta}{\varepsilon_0}\right)^{-3} + \frac{3}{n+2}\left(\frac{\eta}{\varepsilon_0}\right)^{n-1}, & (\eta > \varepsilon_0) \\ 1, (0 \leqslant \eta \leqslant \varepsilon_0) \end{cases} \tag{7}$$

where I is the moment of inertia of the adherend cross-section (per unit width) such that $I = h^3/12$ (rectangular cross-section) and $\eta = h/(2\rho)$. As a check, in the limiting case $\eta = \varepsilon_0$, relation (7) recovers the critical bending moment M_c in relation (5). Given an arbitrary working bending moment M, the radius of curvature ρ of the adherend can be determined by solving the nonlinear Eq. (7) numerically with respect to $1/\rho$ as to be demonstrated in Section 4, and the corresponding maximum axial strain at the top and bottom surfaces of the adherend is $h/(2\rho)$.

After complete unloading due to crack growth as illustrated in Fig. 3, elastic springback happens in the post-fracture adherends of the ABJs. Thus, the radii of curvature measured from the post-fracture adherends (after elastic springback) become larger than those at the maximum working moment. By assuming the radius of curvature of an adherend after complete elastic springback (*i.e.*, complete unloading) to be ρ_0, the recovered elastic strain is

$$\Delta\varepsilon = y\left(\frac{1}{\rho_m} - \frac{1}{\rho_0}\right), \tag{8}$$

where ρ_m is the radius of curvature of the neutral axis of the adherend at the maximum working moment. Therefore, for a material point of location y at a strain-hardening state (σ, ε) such that $\sigma > \sigma_0$ and $\varepsilon > \varepsilon_0$, the residual plastic strain ε_p can be determined according to the strain-stress relation in Fig. 3:

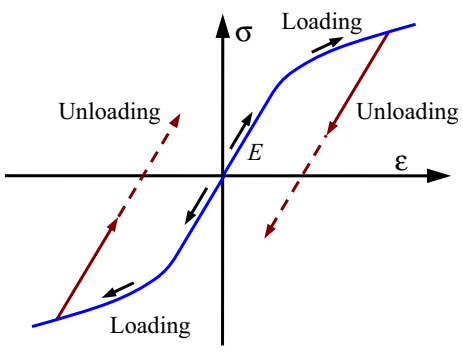

Fig. 3. Schematic diagram of the stress-strain relation of elastoplastic materials with power-law strain-hardening under loading and unloading.

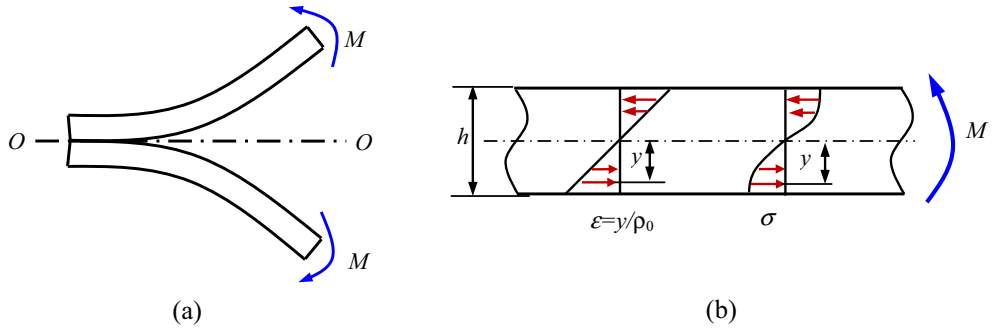

Fig. 4. Adhesively bonded double cantilever beam (DCB) under the action of pure bending moment M: (*a*) Specimen loading configuration and (*b*) Schematic strain and stress distributions across the beam thickness.

$$\varepsilon_p = \frac{y}{\rho_m} - \frac{1}{\varepsilon_0^{n-1}}\left(\frac{y}{\rho_m}\right)^n. \tag{9}$$

In the limiting case of linearly elastic material, *i.e.*, $n = 1$, it leads to $\varepsilon_p = 0$ as expected. After complete unloading, the net bending-moment resultant in any cross-section of the adherends must be zero as the result of bending-moment self-equilibrium at each cross-section, *i.e.*,

$$\int_{-y_c}^{y_c} E\varepsilon y dy + 2\int_{y_c}^{h/2} E(\varepsilon - \varepsilon_p) y dy = 0, \tag{10}$$

where y_c is the critical location specified in Eq. (6) for ρ_m, and ε is the linear axial (flexural) strain:

$$\varepsilon = y/\rho_0. \tag{11}$$

It can be observed from relation (10) that after complete unloading, the elastic region near the neutral axis of the adherends still keeps the similar stress state though the stress level diminishes. However, the elastoplastic region far from the elastic region switches the stress direction to maintain the global bending moment-free of the adherend cross-section.

Substitution of Eqs. (9) and (11) into Eq. (10) yields the relation for determining the radius of curvature ρ_0 of the neutral axis of the adherends after elastic springback as

$$\frac{\eta_0}{\eta_m} = 1 - \left(1 - \frac{3}{n+2}\right)\left(\frac{\eta_m}{\varepsilon_0}\right)^{-3} - \frac{3}{n+2}\left(\frac{\eta_m}{\varepsilon_0}\right)^{n-1}, \tag{12}$$

where $\eta_m = h/(2\rho_m)$ and $\eta_0 = h/(2\rho_0)$. As a check, in the limiting case of linearly elastic material, *i.e.*, $n = 1$, it leads to $\eta_m/\eta_0 \to 0$, *i.e.*, $\rho_0 \to \infty$, and the ABJ adherends recover their initial straight state after purely elastic unloading. The radius of curvature ρ_0 in Eq. (12) is measured from each post-fracture adherend after complete elastic springback. Given a radius of curvature ρ ($\rho_m < \rho < \rho_0$) in the unloading process, the corresponding bending moment per unit width can be determined similar to relation (7) as

$$\frac{M(\rho)}{EI/\rho_m} = \left(\frac{\eta}{\eta_m} - 1\right) + \left(1 - \frac{3}{n+2}\right)\left(\frac{\eta_m}{\varepsilon_0}\right)^{-3} + \frac{3}{n+2}\left(\frac{\eta_m}{\varepsilon_0}\right)^{n-1}, \tag{13}$$

where $\eta = h/(2\rho)$. In the limiting case of linearly elastic material, *i.e.*, $n = 1$, it reads

$$M(\rho) = \frac{Eh^3}{12\rho}, \tag{14}$$

as expected. With the measured radius of curvature ρ_0 of the fractured adherends after complete springback, relation (12) can be employed for determining the radius of curvature ρ_m at the maximum working moment implicitly, and relations (7) and (13) are the moment-curvature relations during loading and unloading processes, respectively.

3. Fracture toughness of plastically deformed ABJs

Based on the fracture testing configuration, the fracture toughness of an elastoplastically deformed ABJ can be expressed as

$$\Gamma = \frac{\Delta W_1 + \Delta W_2 - \Delta U_1 - \Delta U_2}{\Delta l}, \tag{15}$$

where ΔW_i and ΔU_i ($i = 1, 2$) are the work done by the external working moment M and the strain energy stored in each adherend of the ABJ per unit width, respectively, for a crack growth Δl. Since the impact fracture test is a steady dynamic process, the maximum working moment can be determined by Eq. (7) for $\rho = \rho_m$. Thus, in relation (15), the work ΔW done by the working moment M in each adherend (per unit width) for a crack growth Δl is

$$\frac{\Delta W}{Eh\Delta l} = \left(\frac{1}{3} - \frac{1}{n+2}\right)\varepsilon_0^2\left(\frac{\eta_m}{\varepsilon_0}\right)^{-1} + \frac{1}{n+2}\varepsilon_0^2\left(\frac{\eta_m}{\varepsilon_0}\right)^{n+1}. \tag{16}$$

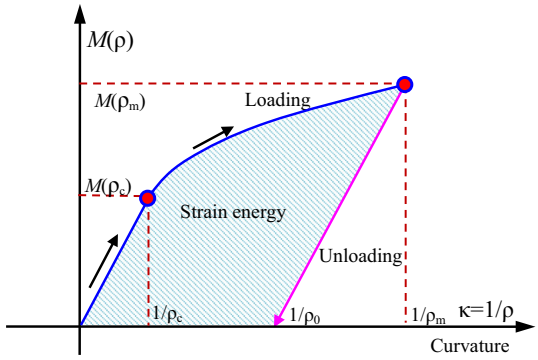

Fig. 5. Schematic diagram of the loading and unloading moment-curvature relation of the elastoplastic ABJ adherends in a steady dynamic fracture test.

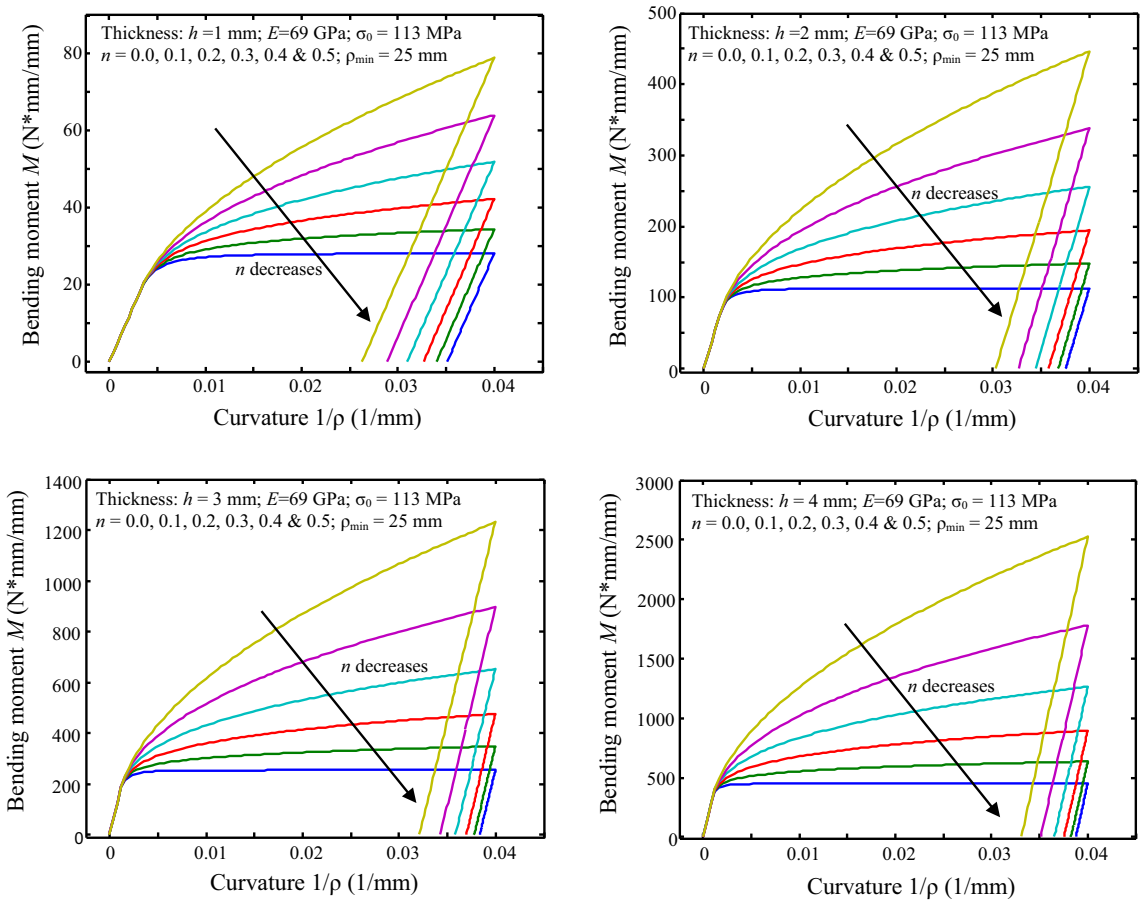

Fig. 6. The loading and unloading moment-curvature diagrams of aluminum-alloy adherends with varying thickness and material strain-hardening index n (unit adherend width).

Correspondingly, the strain energy ΔU stored in each adherend of the ABJs (per unit width) after complete elastic springback due to crack growth Δl can be expressed as

$$\Delta U = \left[\int_{\infty}^{\rho_c} \frac{Eh^3}{12\rho} d\left(\frac{1}{\rho}\right) + \int_{\rho_c}^{\rho_m} M(\rho) d\left(\frac{1}{\rho}\right) - \frac{1}{2} M(\rho_m)\left(\frac{1}{\rho_m} - \frac{1}{\rho_0}\right)\right]\Delta l, \tag{17}$$

where $\rho_0 = h/(2\varepsilon_0)$ is the critical radius of curvature to initiate plastic deformation in the adherends, $\varepsilon_0 = \sigma_0/E$ is the yield strain of the adherends, and $M(\rho_m)$ is the working moment at the minimum radius of curvature ρ_m, *i.e.*, the maximum working moment to drive the facture event. The strain energy integration (17) is illustrated in Fig. 5, in which the 1st term is the strain energy stored in the linearly elastic loading region, the 2nd term is the strain energy stored in the strain-hardening loading region with $M(\rho)$ specified in relation (7), and the 3rd term is the strain energy release in the springback region with $M(\rho)$ specified in relation (13). These three terms correspond to the entire elastoplastic deformation process of the cross-section of the ABJ adherends during the crack growth in the steady dynamic fracture test. Substitution of relations (7) and (12) into Eq. (17) yields the total strain energy ΔU stored in the each adherend of the ABJs per unit width after complete elastic springback as

$$\frac{\Delta U}{Eh\Delta l} = \frac{\varepsilon_0^2}{6} + \frac{\varepsilon_0^2}{3}\left\{-\varepsilon_0\left(1 - \frac{3}{n+2}\right)(\eta_m^{-1} - \eta_c^{-1}) + \frac{3}{(n+1)(n+2)}\varepsilon_0^{-(n+1)}\left[\eta_m^{(n+1)} - \eta_c^{(n+1)}\right]\right\}$$
$$-\frac{1}{6}\eta_m(\eta_m - \eta_0)\left[\left(1 - \frac{3}{n+2}\right)\varepsilon_0^3\eta_m^{-3} + \frac{3}{n+2}\varepsilon_0^{-n+1}\eta_m^{n-1}\right], \tag{18}$$

where $\eta_m = h/(2\rho_m)$, $\eta_0 = h/(2\rho_0)$, and ρ_0 is the radius of curvature of the fractured adherend that is measured from the post-fracture adherend after complete elastic springback. Substitution of relations (16) and (18) for both adherends into Eq. (15)

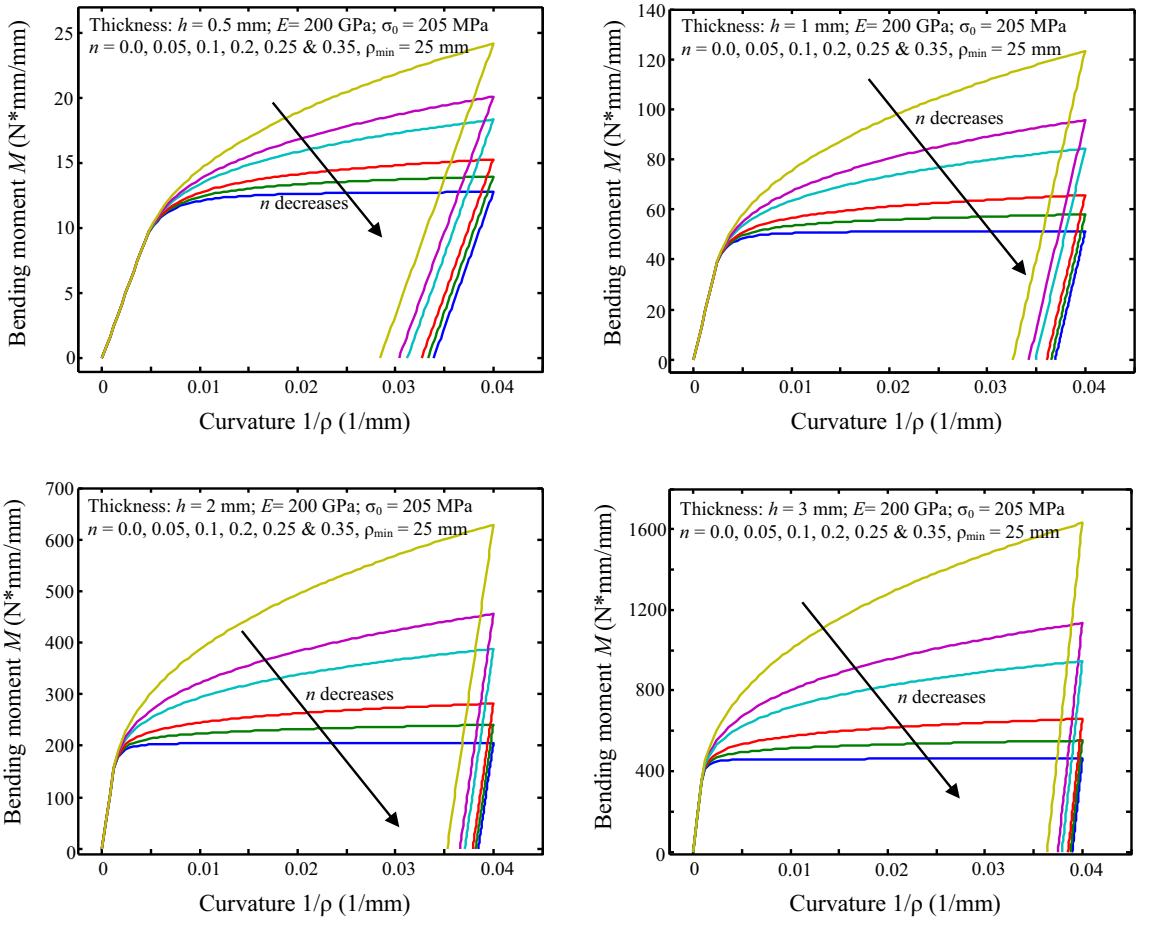

Fig. 7. The loading and unloading moment-curvature diagrams of mild-steel adherends with varying thickness and material strain-hardening index n (unit adherend width).

yields the fracture toughness of the ABJs, which is the energy dissipated by the adhesive layer to generate a unit-area crack growth. In the particular case of the ABJs made of two identical adherends, the fracture toughness (15) can be recast as

$$\begin{aligned}\frac{\Gamma}{2Eh} = &\left(\frac{1}{3}-\frac{1}{n+2}\right)\varepsilon_0^3\eta_m^{-1}+\frac{1}{n+2}\varepsilon_0^{-n+1}\eta_m^{n+1}-\frac{\varepsilon_0^2}{6}\\ &-\frac{\varepsilon_0^2}{3}\left\{-\varepsilon_0\left(1-\frac{3}{n+2}\right)(\eta_m^{-1}-\eta_c^{-1})+\frac{3}{(n+1)(n+2)}\varepsilon_0^{-(n+1)}\left[\eta_m^{(n+1)}-\eta_c^{(n+1)}\right]\right\}\\ &-\frac{1}{6}\eta_m(\eta_m-\eta_0)\left[\left(1-\frac{3}{n+2}\right)\varepsilon_0^3\eta_m^{-3}+\frac{3}{n+2}\varepsilon_0^{-n+1}\eta_m^{n-1}\right],\end{aligned} \tag{19}$$

which is the improved version of the fracture toughness (1) after taking into account the power-law hardening material model (3) and complete elastic springback after unloading.

Compared to the fracture toughness (1) formulated by Thouless et al. [26], the present fracture toughness (19) carries multiple terms due to the use of a piecewise power-law strain-hardening material model (3) and taking into account the entire loading and unloading path of the elastoplastic materials. The present expression (19) is expected to improve the accuracy for extracting the fracture toughness of ABJs of thin ductile plates with large plastic deformation and elastic springback. To apply relation (19) for fracture data reduction, it is needed to first solve the nonlinear algebraic equation (12) to determine the minimum radius of curvature ρ_m at the steady working moment M, *i.e.*, the maximum working moment, based on the radius of curvature ρ_0 measured from the post-fracture adherends after complete springback. Eq. (12) can be solved conveniently by evoking the numerical algorithms for solving single nonlinear algebraic equations such as the

Table 1
Fracture toughness of aluminum-bonded adhesives *A* (LMD1142), *B* (XD3600) and *C* (Esses 73,301). Test data of the adherend thickness, strain-hardening index *n*, and radii of the aluminum adherends after tests were from [26].

h (mm)	Strain-hardening index n	R_p (mm)	Γ (kJ/m^2) [26]	Γ (kJ/m^2) [36]	Γ (kJ/m^2) (Present Model)
Adhesive A					
1.01	0.271	10	1.69 ± 0.25	3.2	3.77 ± 0.09
2.00	0.227	27	1.97 ± 0.30	4.8	4.39 ± 0.10
3.00	0.238	60	1.94 ± 0.29	4.6	4.97 ± 0.28
Adhesive B					
1.01	0.271	13	1.33 ± 0.20	2.4	3.08 ± 0.16
2.00	0.227	36	1.36 ± 0.21	3.0	3.36 ± 0.09
3.00	0.238	78	1.43 ± 0.21	3.1	4.09 ± 0.17
Adhesive C					
1.01	0.271	18	0.83 ± 0.12	1.4	2.19 ± 0.07
2.00	0.227	32	0.89 ± 0.13	1.7	2.52 ± 0.08
3.00	0.238	111	0.92 ± 0.20	1.8	3.13 ± 0.20

Note: R_p is the weighted mean radius used by Thouless et al. [26] and Williams [27]. The fracture toughness (15) based on the present model is calculated directly using the measured radii of curvature of the aluminum-alloy adherends with σ_0 = 113 MPa and E = 69 GPa. The Γ deviation in the present model is obtained by analyzing all the sample data in each test case [26].

Table 2
Fracture toughness of steel-bonded adhesives *A* (LMD1142), *B* (XD3600) and *C* (Esses 73,301). Test data of the adherend thickness, strain-hardening index *n*, and radii of the steel adherend after tests were from [26].

h (mm)	Strain-hardening index n	R_p (mm)	Γ (kJ/m^2) [26]	Γ (kJ/m^2) [27]	Γ (kJ/m^2) (Present model)
Adhesive A					
0.91	0.158	12	1.14 ± 0.17	2.7	2.23 ± 0.09
1.14	0.131	16	1.14 ± 0.17	3.4	2.15 ± 0.10
1.41	0.124	22	1.33 ± 0.20	4.4	2.26 ± 0.09
Adhesive B					
0.71	0.152	11	0.71 ± 0.11	1.5	1.45 ± 0.09
1.14	0.131	21	0.83 ± 0.12	2.2	1.73 ± 0.07
1.41	0.124	37	0.79 ± 0.12	2.0	1.63 ± 0.10
Adhesive C					
0.52	0.094	10	0.33 ± 0.05	0.8	0.55 ± 0.02
0.91	0.158	28	0.42 ± 0.06	0.7	1.11 ± 0.05
1.41	0.124	75	0.34 ± 0.10	0.7	1.28 ± 0.13

Note: R_p is the weighted mean radius used by Thouless et al. [26] and William [27]. The fracture toughness (15) based on the present model is calculated directly using the measured radii of curvature of steel adherends with σ_0 = 205 MPa and E = 200 GPa. The Γ deviation in the present model is obtained by analyzing all the sample data in each test case [26].

popular Newton-Raphson method. With available ρ_m and ρ_0, the work ΔW done by the working moment M and the strain energy ΔU stored in each adherend after crack growth Δl can be determined by relations (16) and (18), respectively.

4. Model applications for experimental data reduction and scaling analysis of ABJ fracture

Let us first examine the dependency of the loading and unloading moment-curvature diagrams upon the material properties and ABJ geometries at a fixed maximum curvature $1/\rho_m$. To do so, adherends of aluminum alloy (Young's modulus E = 69 GPa, yield stress σ_0 = 113 MPa, strain-hardening index n = 0.0, 0.1, 0.2, 0.3, 0.4 and 0.5, and adherend thickness h = 1, 2, 3, and 4 mm) and mild steel (E = 200 GPa, σ_0 = 205 MPa, n = 0.0, 0.05, 0.1, 0.2, 0.25, and 0.35, and h = 0.5, 1, 2, and 3 mm) with unit width are considered. The minimum radius of curvature ρ_{min} of the ABJ adherends at the maximum bending moment M (ρ_{min}) is assumed as 25 mm. These material and geometrical parameters as well as the loading level in term of ρ_{min} are in the range of the experimental studies as reported in the literature [26]. Numerical simulations are made by using the loading and unloading moment-curvature relations (7) and (13).

Figs. 6 and 7 show the moment-curvature diagrams of aluminum-alloy and mild-steel adherends, respectively. It can be observed that both types of adherends have the similar graphical moment-curvature relations, each of which consists of three ranges, *i.e.*, the linearly elastic loading, nonlinear loading, and linearly elastic unloading (elastic springback). Given the strain-hardening index n, the bending moment M increases rapidly with increasing adherend thickness h at a fixed adherend curvature $1/\rho$. In addition, given the value of h, M decreases rapidly with decreasing n at a fixed $1/\rho$, which is due to the softening of the material with decreasing n. In particular, when n = 0, *i.e.*, in the case of an idealized elastoplastic material, M tends to constant after initial yielding. Furthermore, after complete unloading, the springback effect decreases with decreasing n, *i.e.*, a larger value of n corresponds to a relatively larger elastic springback and strain energy release in the elastic unloading stage.

In addition, the fracture toughness (19) developed in the present study is further used to extract the fracture toughness of plastically deformed ABJs based on the fracture test data reported in the literature [26], in which extensive steady dynamic

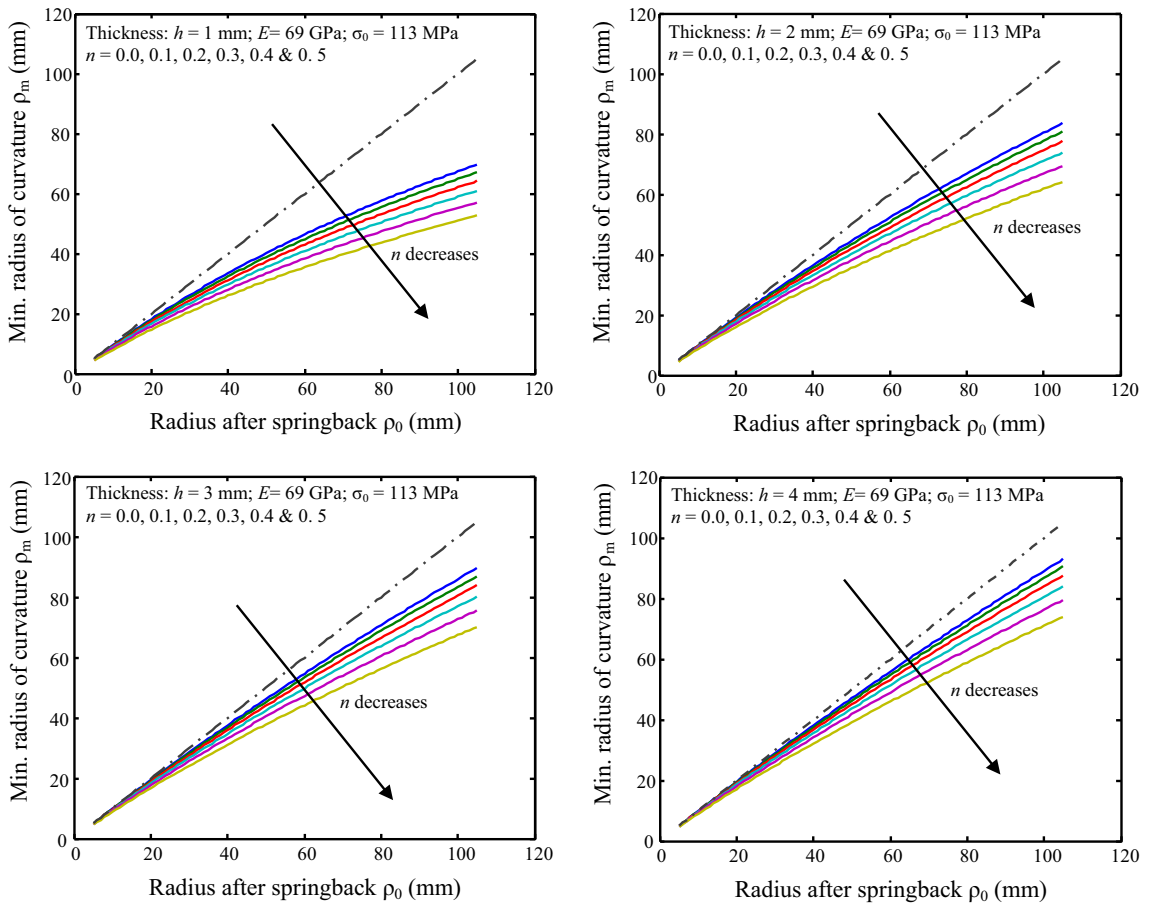

Fig. 8. Variation of the minimum radius of curvature ρ_{min} with respect to the radius of curvature ρ_0 after springback of aluminum-alloy adherends with varying thickness and material strain-hardening index n (Dashed line represents the diagonal for reference).

fracture tests of ABJs made of both thin aluminum-alloy and mild-steel plates were performed as aforementioned. Yet, model parameters of power-law strain-hardening solids according to the constitutive law (3) are not exhausted for the particular aluminum-alloy and mild-steel plates used in these fracture tests. In the following, the mechanical properties of the aluminum-alloy plates are selected as Young's modulus $E = 69 \pm 5$ GPa and yield stress $\sigma_0 = 113 \pm 3$ MPa, which were used for the fracture analysis of the same ABJs in the literature [26,40], and the strain-hardening index n was directly selected from the nonlinear elastic material model (2) by fitting the test data [26]. Such a choice is due to lack of original experimental data to fit the model parameters of the present elastoplastic material model (3) and may not lead to appreciable deviation between material model (3) and the nonlinear elastic material model (2) in the loading range. For cold-rolled mild-steel plates, $E = 200$ GPa, $\sigma_0 = 170$–240 MPa, and n was also selected from the nonlinear elastic material model (2) in the literature [26].

Based on the available radii of curvature of the two individual adherends of the ABJ specimens after complete springback, relation (12) is used to determine the minimum radius ρ_m of curvature of each adherend at the maximum working moment $M(\rho_m)$; relation (19) is used to extract the fracture toughness of the ABJs. The values of fracture toughness for the ABJs made of thin aluminum-alloy and mild-steel plates with varying adherend thickness are tabulated in Tables 1 and 2, in which the fracture toughness (19) is determined by using the mean values of the mechanical properties of the aluminum-alloy ($\sigma_0 = 113$ MPa and $E = 69$ GPa) and mild-steel plates ($\sigma_0 = 205$ MPa and $E = 200$ GPa) and all the measured radii of curvature of the adherends after springback by Thouless et al. [26]. For the purpose of comparison, Williams's corrections by assuming a root rotation at the adherend end were also listed in Tables 1 and 2 [27,36,37]. It is worthy to mention that similar to those reported by Thouless et al. [26], Williams's corrections were also based on the nonlinear elastic material model (2). It can be found in Tables 1 and 2 that the present model predicts quite a few values of fracture toughness close to Williams's corrections, nearly double the values of fracture toughness reported by Thouless et al. [26], which are considered as the true fracture toughness of the ABJs with Thouless's argument [26] and also used as references for the purpose of comparison in this study. In particular, the present model predicts the values of fracture toughness of adhesives A and B based on ABJs

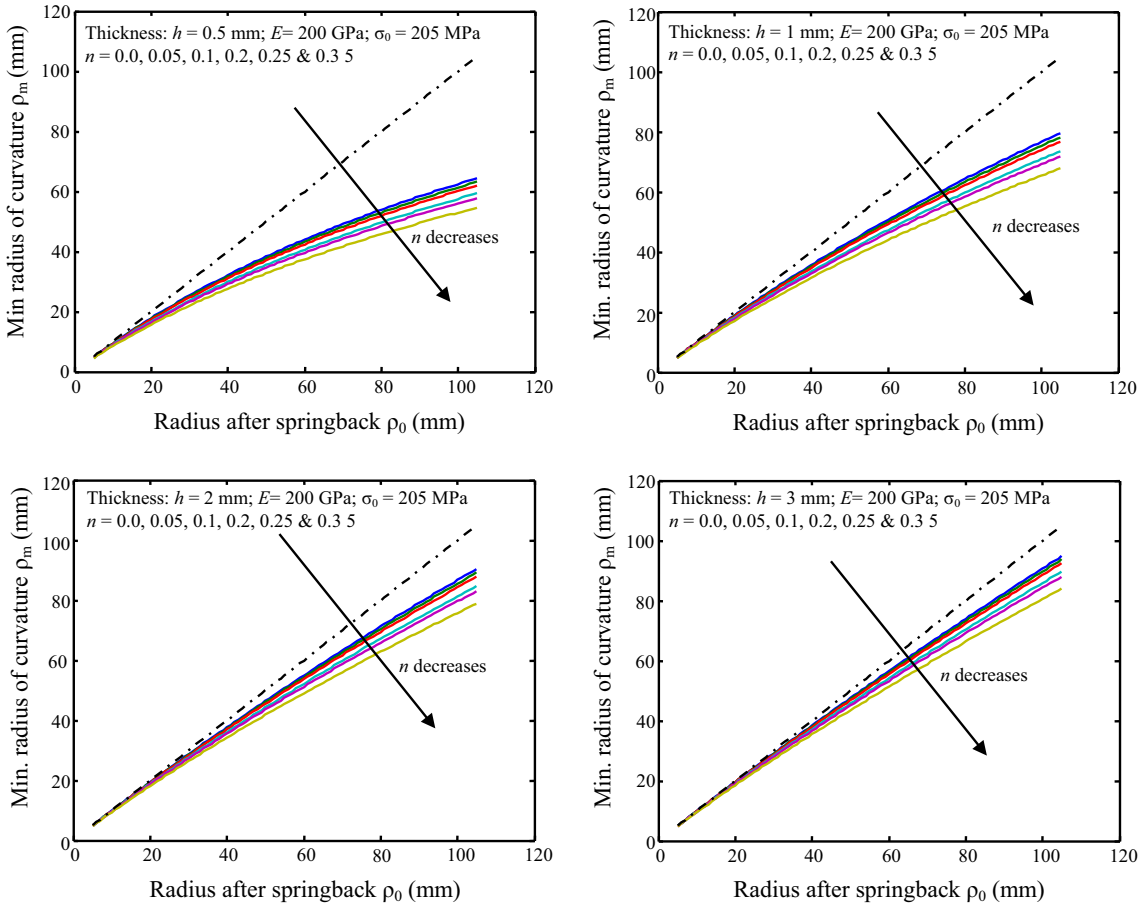

Fig. 9. Variation of the minimum radius of curvature ρ_{min} with respect to the radius of curvature ρ_0 after springback of mild-steel adherends with varying thickness and material strain-hardening index n (Dashed line represents the diagonal for reference).

made of thin steel plates, as listed in Table 2, very close to double the values of fracture toughness provided by Thouless et al. [26] and even closer than those provided by Williams's corrections [27,36,37].

Yet, the present model also predicts a few obvious overshot values of the fracture toughness of the three adhesives based on aluminum-alloy ABJs. For example, in Table 1 the present model predicts the values of fracture toughness with the maximum deviations for adhesives *A*, *B* and *C* based on ABJs made of 3 mm thick aluminum-alloy adherends as 4.97 ± 0.28 kJ/m^2, 4.09 ± 0.17 kJ/m^2, and 3.13 ± 0.20 kJ/m^2, respectively, which are 28%, 43%, and 70% higher than double the values of the fracture toughness reported in the literature [26]. Such large deviations might be related to the deviation of selected model parameters in the present material model (3) for the aluminum alloy sheets as such model parameters were not available in the literature. For example, due to lack of the experimental stress-strain diagrams of aluminum alloy and steel plates, the exponent *n* of the nonlinear elastic material model (2), which was fitted from experimental data [26], was directly used as the strain-hardening index *n* of the present material model (3). Noticeable deviations may exist for the parameter *n* between the two material models. As an example, here a brief investigation is made on the parameter dependency of the fracture toughness of the ABJs made of 1 mm thick aluminum-alloy sheets. In this case, if slightly scaling down the parameter *n* from 0.271, which was obtained by fitting the experimental data based on the material model (2) in the literature [26] and was used in the present material model (3) to generate the results in Table 1, to 0.271/1.08 = 0.251, the present model (19) predicts the values of fracture toughness of adhesives *A*, *B* and *C* as 3.33 ± 0.08 kJ/m^2, 2.73 ± 0.14 kJ/m^2, 1.96 ± 0.06 kJ/m^2, which are much close to double the values of fracture toughness obtained in the steady dynamic fracture tests [26] as also listed in Table 1.

Therefore, the present model is capable of extracting reliable fracture toughness from steady dynamic fracture tests of ABJs with large plastic deformations, provided that the materials behave following power-law strain-hardening solids (3) and sufficient experimental data are available to fit the model parameters *E*, σ_0 and *n*. Other potential influencing factors responsible for the deviations between the present model predictions and experimental data could be the test data collection, failure mechanisms out of the assumption of pure bending, friction between the wedge and adherends, or the strain energy dissipation not fully used for driving crack growth such as heat and kinetic energy, among others.

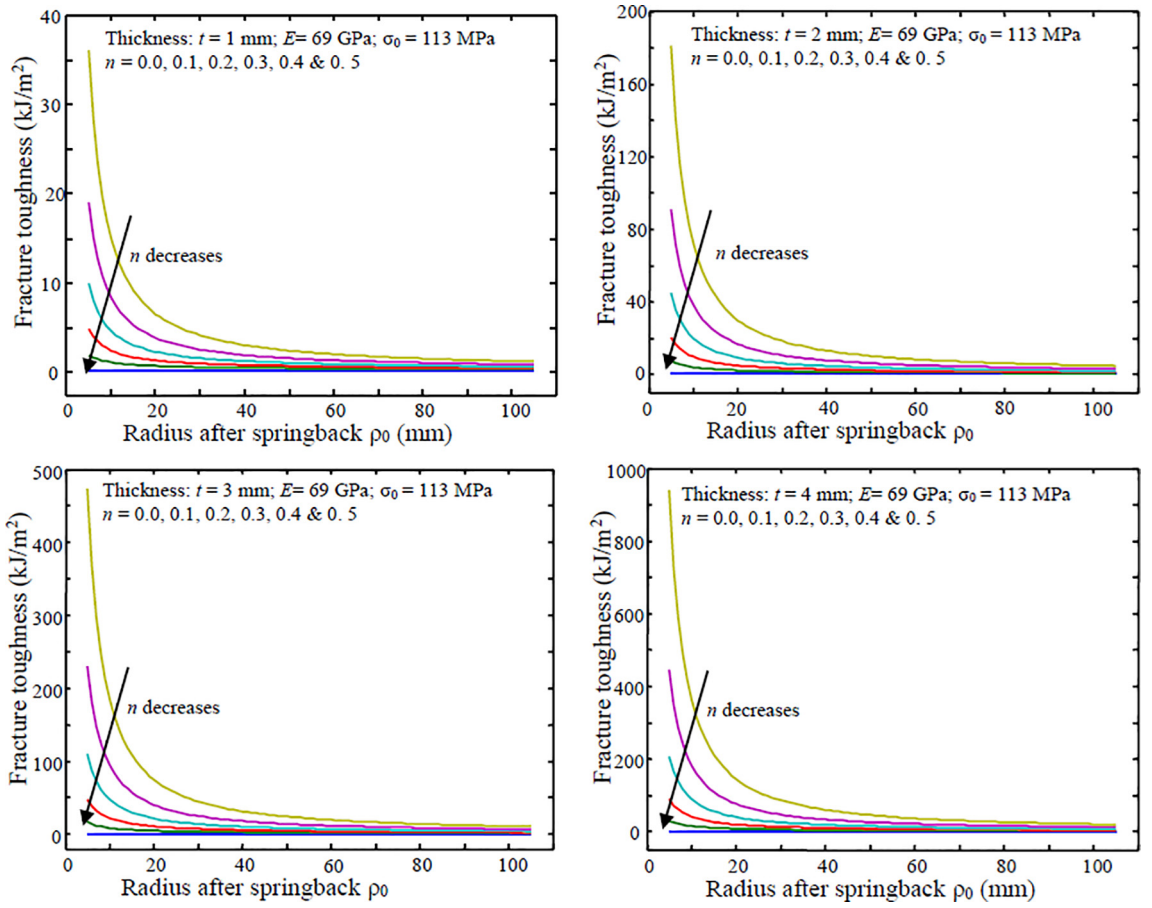

Fig. 10. Variation of the fracture toughness Γ with respect to the radius of curvature ρ_0 after springback of ABJs of thin aluminum-alloy plates with varying thickness and material strain-hardening index *n*.

Moreover, the present model is further used for scaling analysis of the springback and fracture toughness of ABJs made of thin aluminum-alloy and mild-steel plates with varying strain-hardening index n at varying ρ_0. Figs. 8 and 9 are the variations of the minimum radius ρ_m at the maximum working moment $M(\rho_m)$ with respect to ρ_0 of the ABJ adherends after complete springback, in which the material properties and geometries are selected as the same as those employed in Figs. 6 and 7. The general varying tendencies are similar for both types of ABJs. Given the values of ρ_0 and the adherend thickness h, ρ_m decreases with decreasing n. This is due to the fact that a lower value of n indicates a more plastically deformed ABJ, *i.e.*, a lower value of ρ_m. In addition, at the fixed values of ρ_0 and n, ρ_m increases with increasing h, *i.e.*, thicker elastoplastic specimens tending to more noticeable springback. In the limiting case of idealized elastoplastic materials ($n = 0$), the minimum springback exhibits. In contrast, in the limiting case of linearly elastic materials ($n = 1$) or nonlinear elastic materials, the adherends completely recover the original configurations after unloading, *i.e.*, the maximum springback.

Figs. 10 and 11 are the corresponding variations of the fracture toughness Γ with respect to the radius ρ_0 for ABJs of thin aluminum-alloy and mild-steel plates, respectively, in which the material properties and geometries are selected as the same as those considered in Figs. 8 and 9 and the two adherends of the ABJ specimens are treated to be identical. The general varying tendencies are similar to both types of the ABJs. In each case, Γ decreases rapidly with increasing ρ_0. In addition, given the values of ρ_0 and h, Γ decreases with decreasing n. This is due to the fact that a larger value of n (stiffer) implies that a larger $M(\rho_m)$ is needed to generate the given ρ_0. Moreover, given the values of ρ_0 and n, Γ increases rapidly with increasing h, *i.e.*, a thicker elastoplastic ABJ specimen tends to a higher fracture toughness Γ due to a larger $M(\rho_m)$ needed to derive the crack growth. It is worthy to mention that such a scaling comparison is based on the assumption that the fracture toughness Γ is a material constant, which is independent of external loads and specimen geometries, and the scaling properties of Γ in above represents the possible experimental observation of fracture tests of ABJ specimens made of materials with varying fracture toughness and geometries such as varying adherend thickness h.

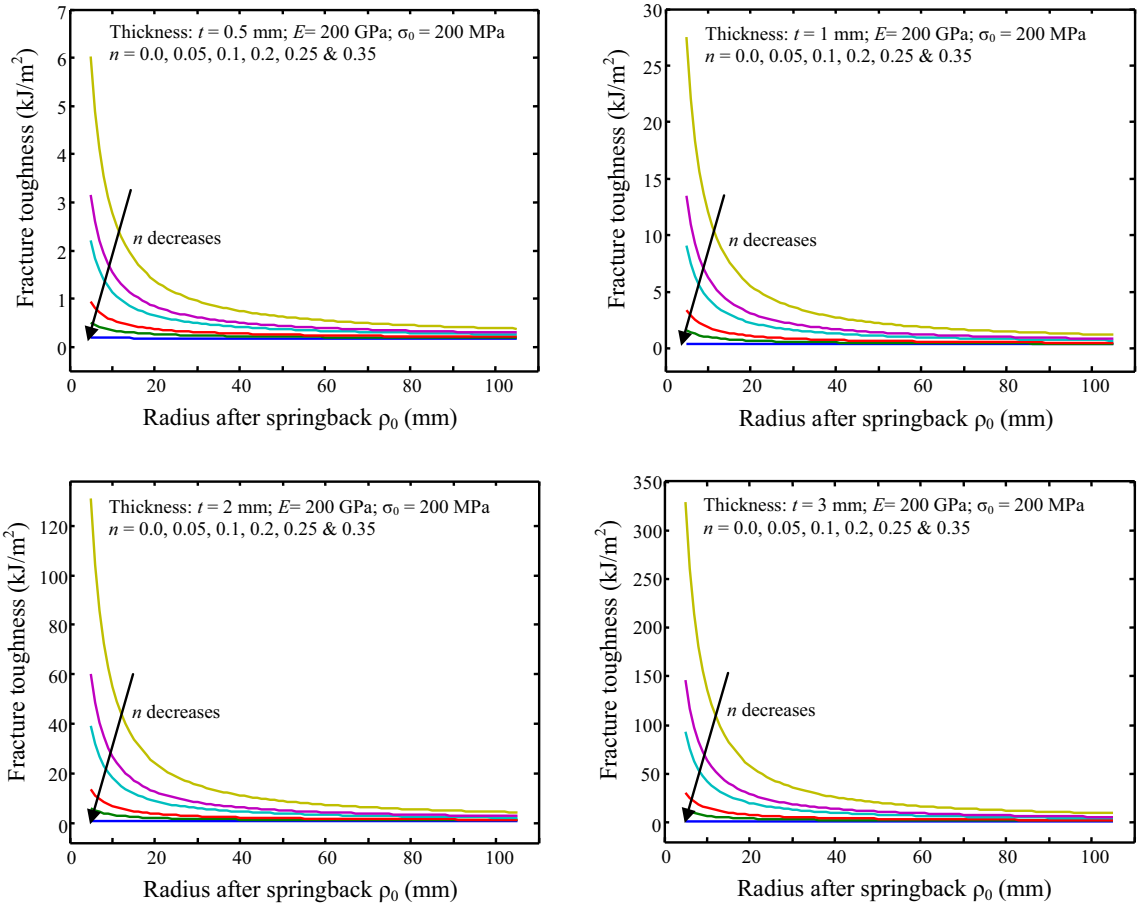

Fig. 11. Variation of the fracture toughness Γ with respect to the radius of curvature ρ_0 after springback of ABJs of thin mild-steel plates with varying thickness and material strain-hardening index n.

5. Concluding remarks

An elastoplastic fracture mechanics model has been formulated for determining the fracture toughness of aluminum-alloy and mild-steel ABJs with large plastic deformations and elastic springback. Based on the present model, the maximum curvature $(1/\rho_m)$ and corresponding maximum working bending moment $M(\rho_m)$ can be determined explicitly from the measured radius of curvature $(1/\rho_0)$ of the ABJ specimens after complete elastic springback, which are appreciably different from those based only on nonlinear elastic material model (2) without springback. The stored strain energy in the ABJ adherends has been determined in explicit form, which consists of the strain energy stored in the entire stage of loading and unloading, *i.e.*, the linearly elastic loading, nonlinear loading, and linearly elastic unloading range. Without additional *ad hoc* assumptions and simplifications beyond the elastoplastic constitutive law (3) of power-law strain-hardening materials and linearly varying axial strain across the adherend thickness (*i.e.*, *Euler-Bernoulli beam*), the present model is capable of extracting the reliable fracture toughness of ABJs with large plastic deformations from steady dynamic fracture test data. This present model has its advantages: (1) The elastoplastic power-law strain-hardening material model is more general and close to the mechanical performance of many practical ductile metals extensively used in engineering including aluminum alloys and mild steels; (2) The maximum working moment $M(\rho_m)$ to drive the crack growth in ABJs is determined accurately with taking into account the elastic springback of the ABJ adherends; (3) The effect of elastic springback after complete unloading has been considered for determining the maximum curvature $(1/\rho_m)$, corresponding to the maximum working bending moment $M(\rho_m)$ and the maximum strain energy stored in the plastically deformed ABJs.

Furthermore, the present model has also been utilized for detailed scaling analysis to examine effects of the mechanical properties and joint geometries on the elastic springback and fracture toughness of ABJs at varying loading level, which is useful to explore the effects of governing parameters on the fracture behavior of plastically deformed ABJs and design of metal ABJ specimens for better testing and fracture data reduction. The present model can be used for the analysis of broader fracture and adhesive failure events of thin beams and film structures of ductile metals with large plastic deformations and elastic springback such as peeling tests in coatings, fracture tests of ductile metals, and machine cutting of ductile metals, among others.

Acknowledgment

Partial support of the research by the NASA EPSCoR (NASA Grant #NNX07AK81A, seed grant: 43500-2490-FAR018640), NDSU Development Foundation (Grant No.: 43500-2490-FAR0017475), and NDSU Faculty Research Initial Grant is gratefully appreciated.

Appendix A. Supplementary material

Supplementary data associated with this article can be found, in the online version, at https://doi.org/10.1016/j.engfracmech.2017.11.040.

References

[1] Park SY, Choi WJ, Choi HS, Kwon H, Kim SH. Recent trends in surface treatment technologies for airframe adhesive bonding processing: a review (1995–2008). J Adhes 2010;86:192–221.
[2] Davis M, Bond D. Principles and practices of adhesive bonded structural joints and repairs. Int J Adhes Adhes 1999;19:91–105.
[3] Higgins A. Adhesive bonding of aircraft structures. Int J Adhes Adhes 2000;20:367–76.
[4] Grant LDR, Adams RD, da Silva LFM. Effect of the temperature on the strength of adhesively bonded single lap and T joints for the automotive industry. Int J Adhes Adhes 2009;29:535–42.
[5] da Silva LFM, das Neves PJC, Adams RD, Spelt JK. Analytic models of adhesively bonded joints-part I: Literature survey. Int J Adhes Adhes 2009;29:319–30.
[6] da Silva LFM, das Neves PC, Adams RD, Wang A, Spelt JK. Analytic models of adhesively bonded joints-part II: Comparative study. Int J Adhes Adhes 2009;29:331–41.
[7] Wu XF, Jenson RA. Stress-function variational method for stress analysis of bonded joints under mechanical and thermal loads. Int J Eng Sci 2011;49:279–94.
[8] Wu XF, Jenson RA. Semi-analytic stress-function variational approach for the interfacial stresses in bonded joints. J Eng Mech 2014;140. 04014089; Wu XF, Zhao YH. Stress-function variational method for interfacial stress analysis of adhesively bonded joints. Int J Solids Struct 2013;50:4305–19.
[9] Wu XF, Jenson RA, Zhao YH. Stress-function variational approach to the interfacial stresses and progressive cracking in surface coatings. Mech Mater 2014; 69: 195–203.
[10] Carlsson LA, Pipes RB. Experimental characterization of advanced composite materials. New Jersey: Prentice-Hall; 1987.
[11] Johnson WS. Adhesively bonded joints: testing, analysis, and design. ASTM STP 981, Philadelphia: ASTM; 1988.
[12] Mittal KL. Adhesive joints: formation, characteristics and testing. Boston: Brill Academic Publishers; 2003.
[13] Wu XF, Yarin AL. Recent progress in interfacial toughening and damage self-healing of polymer composites based on electropsun and solution-blown nanofibers: an overview. J Appl Polym Sci 2013;130:2225–37.
[14] Suo ZG, Hutchinson JW. Interface crack between two elastic layers. Int J Fract 1990;43:1–18.
[15] Hutchinson JW, Suo Z. Mixed mode cracking in layered materials. Adv Appl Mech 1992;29:64–191.
[16] Schapery RA, Davidson BD. Prediction of energy release rate for mixed-mode delamination using classical plate theory. ASME Appl Mech Rev 1990;43:S281–7.
[17] Davidson BD, Hu HR, Schapery RA. An analytical crack-tip element for layered elastic structures. J Appl Mech-Trans ASME 1995;62:294–305.
[18] Sundararaman V, Davidson BD. An unsymmetric double cantilever beam test for interfacial fracture toughness determination. Int J Solids Struct 1997;34:799–817.

[19] Wang JL, Qiao PZ. Analysis of beam type fracture specimens with crack-tip deformation. Int J Fract 2005;132:223–48.
[20] Wu XF, Dzenis YA. Closed-form solution for a mode-III interfacial edge crack between two bonded dissimilar elastic strips. Mech Res Commun 2002;29:407–12.
[21] Wu XF, Dzenis YA. Closed-form solution for the size of plastic zone in an edge-cracked strip. Int J Eng Sci 2002;40:1751–9.
[22] Wu XF, Dzenis YA, Fan TY. Two semi-infinite interfacial cracks between two bonded dissimilar elastic strips. Int J Eng Sci 2003;41:1699–710.
[23] Wu XF, Lilla E, Zou WS. A semi-infinite interfacial crack between two bonded dissimilar elastic strips. Arch Appl Mech 2002;72:630–6.
[24] Kinloch AJ, Lau CC, Williams JG. The peeling of flexible laminates. Int J Fract 1994;66:45–70.
[25] Moidu AK, Sinclair AN, Spelt JK. Analysis of the peel test: prediction of adherend plastic dissipation and extraction of fracture energy of metal-to-metal adhesive joints. J Test Eval 1995;23:241–53.
[26] Thouless MD, Adams JL, Kafkalidis MS, Ward SM, Dickie RA, Westerbeek GL. Determining the toughness of plastically deforming joints. J Mater Sci 1998;33:189–97.
[27] Williams JG. Friction and plasticity effects in wedge splitting and cutting fracture tests. J Mater Sci 1998;33:5351–7.
[28] Yang QD, Thouless MD, Ward SM. Numerical simulations of adhesively-bonded beams failing with extensive plastic deformation. J Mech Phys Solids 1999;47:1337–53.
[29] Yang QD, Thouless MD, Ward SM. Analysis of the symmetrical 90°-peel test with extensive plastic deformation. J Adhes 2000;72:115–32.
[30] Wei YG. Thin layer splitting along the elastic-plastic solid surface. Int J Fract 2002;113:233–52.
[31] Atkins AG. Toughness and cutting: a new way of simultaneously determining ductile fracture toughness and strength. Eng Fract Mech 2005;72:849–60.
[32] Hadavinia H, Kawashita L, Kinloch AJ, Moore DR, Williams JG. A numerical analysis of the elastic-plastic peel test. Eng Fract Mech 2006;73:2324–35.
[33] Williams JG, Patel Y, Blackman BRK. A fracture mechanics analysis of cutting and machining. Eng Fract Mech 2010;77:293–308.
[34] Atkins AG, Chen Z, Cotterell B. The essential work of fracture and J_R curves for the double cantilever beam specimen: an examination of elastoplastic crack propagation. Proc R Soc Lond A-Math Phys Engn Sci 1998;454:815–33.
[35] Li XF, Lee KY. Fracture of a thin power-law nonlinear materials with a crack using the DCB model. Int J Fract 2016;201:119–25.
[36] Kinloch AJ, Williams JG. Comments on "Determining the toughness of plastically deforming joints". J Mater Sci Lett 1998;17:813–4.
[37] Kinloch AJ, Williams JG. Further comments on "Determining the toughness of plastically deforming joints". J Mater Sci Lett 1999;18:2049.
[38] Yang QD, Thouless MD. Reply on 'Comments on "Determining the toughness of plastically deforming joints"'. J Mater Sci Lett 1999;18:2051–3.
[39] Pardoen T, Ferracin T, Landis CM, Delannay F. Constraint effects in adhesive joint fracture. J Mech Phys Solids 2005;53:1951–83.
[40] Cavalli MN, Thouless MD, Yang QD. Cohesive-zone modeling of the deformation and fracture of spot-welded joints. Fatigue Fract Eng Mater Struct 2005;28:861–74.